The effect of hydrogen on the breakdown of the protective oxide scale in solid oxide fuel cell interconnects

Corrosion Science xxx (xxxx) xxx

Contents lists available at ScienceDirect

Corrosion Science

journal homepage: www.elsevier.com/locate/corsci

The effect of hydrogen on the breakdown of the protective oxide scale in solid oxide fuel cell interconnects

Kerem O. Gunduz [a,b], Anton Chyrkin [a], Claudia Goebel [a], Lukas Hansen [a], Oscar Hjorth [a], Jan-Erik Svensson [a], Jan Froitzheim [a,*]

[a] Chalmers University of Technology, Department of Chemistry and Chemical Engineering, Division of Energy and Materials, Kemivägen 10, SE-41296, Gothenburg, Sweden

[b] Gebze Technical University, Department of Materials Science and Engineering, 41400, Gebze, Kocaeli, Turkey

ARTICLE INFO

Keywords:
Solid oxide fuel cell
Interconnect
Corrosion
Dual
Atmosphere
Hydrogen
AISI 441

ABSTRACT

In this study, the effect of hydrogen, on the degradation of AISI 441 interconnect, under solid oxide fuel cell operating conditions was investigated between 500−800 °C for 336 h. As a new hypothesis, it is concluded that, hydrogen impedes Cr diffusion, probably in the grain boundaries, leading to the breakdown of the protective oxide scale. This effect is most severe at 600 °C, while at lower or higher temperatures the effect is attenuated. Cr diffusion is enhanced at high temperatures, whereas protective scales can be obtained at low temperatures with a lower amount of Cr.

1. Introduction

Solid oxide fuel cells (SOFC) have received considerable attention because they combine the typical advantages of fuel cells, such as high electrical efficiency, and silent and mechanically reliable operation, with wide fuel flexibility [1,2]. However, a potential of approximately 1 V can be obtained through one single cell composed of anode, cathode, and electrolyte, which is not sufficient for most applications. Therefore, a fourth component, an interconnect, is used to connect multiple cells electrically in series to form a stack [3–6]. In addition to electrical connection, interconnects also separate the gas compartments of adjacent cells by acting as a physical barrier, thus preventing the mixing of fuel and air and providing the gas channels required for the anode and cathode gases. Owing to the technological improvements in the components of the SOFCs, especially on the electrolyte level, current typical operating temperatures have decreased to 600–800 °C, which gives the opportunity to use metallic materials as interconnects [1]. Among the metallic materials, chromia-forming ferritic stainless steels (FSS) are the most commonly used material because of a combination of moderate oxidation resistance, low cost, ease of formability and manufacturability, good thermal compatibility with the other components of the stack, and relatively low electrical resistivity [3,5]. However, the interconnect contributes significantly to stack cost even with the use of ferritic stainless steels [7]. The interconnect also contributes significantly to cell degradation. The most well-known mechanism for cell degradation is Cr poisoning, where volatile Cr(VI) evaporates from the interconnect surface and deposits on the cathode, blocking electrochemically active sites [8–11]. Another important degradation mechanism is the increase in area specific resistance (ASR) due to the growth of Cr_2O_3. Cr_2O_3 has only moderate conductivity; its growth, particularly at higher temperatures, results in an increase in ASR [12]. Both of these problems can be mitigated by applying protective coatings, which mitigate Cr evaporation and often slow down the growth rate of an oxide scale [13,14]. However, another degradation mechanism specific to SOFC and SOEC-operating conditions is called the dual atmosphere effect, which leads to unusually fast corrosion and premature failure of the interconnects. When an interconnect is placed in a SOFC stack, one side of the interconnect is exposed to air, and the other side is simultaneously exposed to fuel, H_2 for example. The pioneering work of Yang et al. [15] has shown that this scenario leads to very different oxidation on the air side compared to having air on both sides of the steel sheet. Researchers [15–33] have been studying this effect for the past seventeen years. Although it has been firmly established that hydrogen from the fuel side diffuses to the air side and affects air-side oxidation, the mechanism for how hydrogen causes a breakdown of the protective oxide scale has not been established. Also, the severity of the dual atmosphere effect varies

* Corresponding author.
E-mail address: jan.froitzheim@chalmers.se (J. Froitzheim).

https://doi.org/10.1016/j.corsci.2020.109112
Received 24 September 2020; Received in revised form 5 November 2020; Accepted 7 November 2020
Available online 12 November 2020

widely among studies [24,25,28,30]. While most studies on the dual atmosphere effect were carried out at 800 °C or above, a study published by Alnegren et al. [30] has shown that, between 600 and 800 °C the most severe effect was found at 600 °C indicating an inverse temperature relationship. This clearly shows the severity of the problem for SOFC technology as it has gradually moved into this temperature range, especially for intermediate temperature solid oxide fuel cells (IT-SOFC) [34]. The present study analyzed the effect of temperature using Wagner's oxidation theory.

2. Materials and methods

AISI 441 steel plates with 0.2 mm thickness were obtained from Sandvik Materials Technology in bright-annealed condition with a surface roughness of 0.1−0.3 μm. The chemical composition of the steel is given in Table 1.

The steel was punched in order to obtain circular samples with a diameter of 21 mm. Afterwards, the samples were cleaned stepwise with acetone and ethanol for 20 min each in an ultrasonic bath and subsequently dried with synthetic laboratory air. Then the samples were weighed with a six-digit Mettler Toledo XP6 microbalance before pre-oxidation. Pre-oxidation was performed at 800 °C in filtered laboratory air+3 % H_2O for 20 min by placing the samples in a pre-heated tube furnace. The samples were removed from the furnace after 20 min, cooled directly in laboratory air, and weighed again. The mass gain after pre-oxidation was approximately 0.008 mg/cm^2, which is in accordance with the previous study by Goebel et al. [20]. Afterwards, non-pre-oxidized and pre-oxidized samples were placed in a sample holder made of 253 MA steel. Details on the experimental setup are given elsewhere [25,29]. Gold gaskets were used as a sealant to ensure that the system was gas tight. Dual versus single exposures were performed simultaneously in order to compare the effect of H_2 on the air side. The gas composition was Ar–5 % H_2 + 3 % H_2O with a flow rate of 100 sml min^{-1} on the fuel side, while filtered laboratory air+3 % H_2O with a flow rate of 8800 sml min^{-1} was chosen for the air side in order to mimic the conditions found in a real stack. The high flow rate on the air side was chosen in order to be within a flow regime where Cr evaporation is flow independent [9]. The humidity level was controlled with a chilled mirror hygrometer (Michelle-Optidew vision). A heating/cooling rate of 1 °C min^{-1} was used for all exposures to avoid thermal stresses. All exposures were repeated at least once to ensure that the results were reproducible. After 168 h and 336 h of exposure, samples were cooled to room temperature and photographed with a Canon EOS 1D Mk III camera equipped with a Canon 100 f/2.8 macro lens for visual inspection. A Leica TIC 3X broad ion beam miller was employed for the preparation of cross-sections. For scanning electron microscopy and energy dispersive X-ray spectroscopy (SEM-EDX), a FEI ESEM QUANTA 200 equipped with an Oxford X-max 80 EDX detector and a Zeiss LEO Ultra FE-55 equipped with an in-lens detector were used.

3. Results

Photographs of the air side of the samples with and without pre-oxidation exposed under dual and single atmosphere conditions at different temperatures for 336 h are shown in Fig. 1.

All samples exposed in single atmosphere conditions exhibited protective oxide scales, irrespective of pre-oxidation state or temperature. Obviously, the oxide scales formed under single atmosphere conditions were thicker at high temperature, but all oxides were Cr rich and classified as protective.

Fig. 1 shows that non-pre-oxidized samples exposed under dual atmosphere conditions were totally covered with a non-protective oxide scale except for the sample exposed at 500 °C. For the samples exposed at 500 °C, no apparent difference was observed between samples exposed to single or dual atmosphere as both samples exhibited thin protective oxide scales. Considering that all other non-pre-oxidized samples were totally covered with a non-protective oxide scale, it was not possible to determine a temperature dependency effect from a visual inspection of dual atmosphere corrosion.

As for the surfaces of pre-oxidized samples, 600 °C was clearly the most critical temperature where the dual atmosphere effect was the most pronounced and where the most severe corrosion occurred. The surface was completely covered with a non-protective oxide scale only at that temperature, whereas the coverage of the non-protective oxide scale was lower and temperature dependent at lower and higher temperatures. At 500 °C, a dual versus single atmosphere comparison showed that the surfaces seemed identical and completely covered with a protective oxide scale. Spots corresponding to a non-protective oxide were visible all over the surface of the material exposed to dual atmosphere at 550 °C. The sample surface was covered with non-protective oxide as spots at 650 °C, however the spots were larger but fewer in number than the ones observed at 550 °C. A non-protective oxide was present as spots at 700 °C as well. Although these spots were smaller in size than the ones observed at 650 °C, less non-protective oxide coverage was observed at 700 °C than at 650 °C. A dual versus single atmosphere comparison at 800 °C showed that the surfaces were similar, indicating that the effect of dual atmosphere diminished at higher temperature.

Fig. 2 shows the plan view SEM micrographs of the air side of non-pre-oxidized samples exposed under dual atmosphere conditions at different temperatures for 336 h. Fig. 2 shows that all samples were completely covered with a non-protective oxide scale, except for the sample exposed at 500 °C, which was protective. A transition from a surface covered with whiskers to undulated porous surfaces was found as the exposure temperature increased from 550 °C to 800 °C.

Fig. 3 depicts the plan view SEM micrographs of the air side of all pre-oxidized samples. The marking X in Fig. 3 represents the non-protective oxide scale. At 500 °C, the surface of the pre-oxidized sample was completely protective as for the non-pre-oxidized samples (Fig. 2a). At 550 °C (Fig. 3b), iron-rich nodules were found all over the sample surface, however a protective oxide scale also remained, whereas at 600 °C (Fig. 3c), the entire surface was covered with a non-protective oxide scale, as shown in Fig. 1. At 650 °C (Fig. 3d) and at 700 °C (Fig. 3e), the surface was partially covered with a non-protective oxide scale and partially with a protective oxide scale. Similar to the visual inspection, the SEM micrographs also showed that the surface of the sample exposed at 700 °C was covered with a higher percentage of protective oxide than the sample exposed at 650 °C. At 800 °C, the surface was completely covered with a protective oxide scale.

Fig. 4 illustrates the SEM micrographs of cross-sections of the air side of non-pre-oxidized samples exposed under dual atmosphere conditions between 550−800 °C for 336 h, and Fig. 5 illustrates the SEM-EDX mapping of these regions. Cross-sections for samples exposed at 500 °C were not prepared, since a plan view SEM investigation of those samples showed that a protective oxide scale was present, which was too thin for a meaningful investigation in cross-section. Three different temperature-dependent layers were identified based on the information presented in Fig. 4 and Fig. 5. Combining the EDX analysis of the present study with results obtained with TEM in the work performed by Alnegren et al. [29], the top layer at the oxide-gas interface was identified as outward grown Fe_2O_3, the second layer was identified as

Table 1
Chemical composition of the AISI 441 steel used in this study (in weight %).

Material	Fe	Cr	Mn	Si	Ti	Nb	Ni	C	S	P	N
AISI 441/EN 1.4509	Bal.	17.56	0.35	0.59	0.173	0.39	0.26	0.014	0.001	0.03	0.017

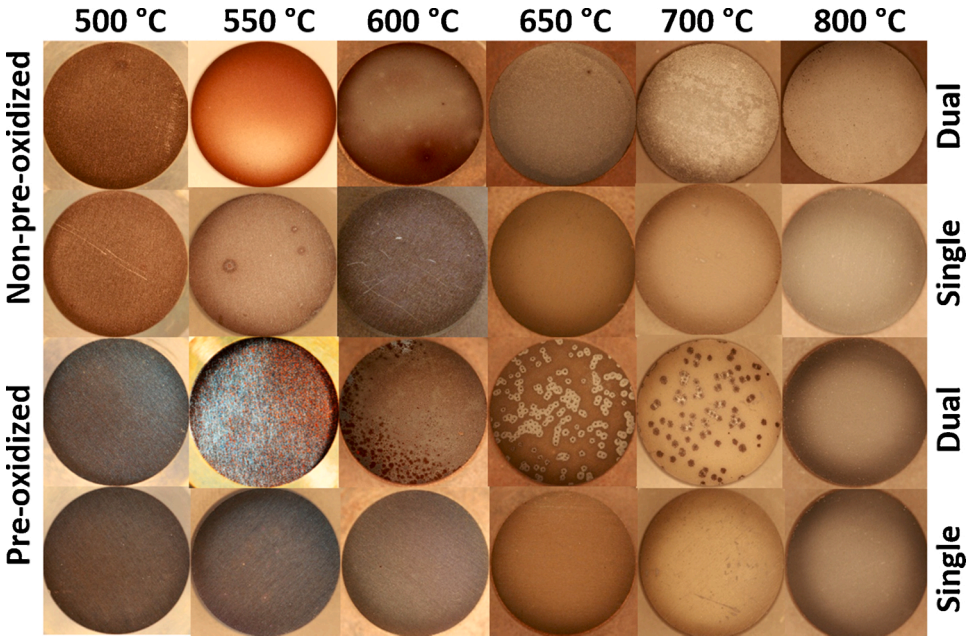

Fig. 1. Photographs of the samples with and without pre-oxidation under dual and single atmosphere conditions at different temperatures after 336 h of exposure.

internally grown $(Fe,Cr)_3O_4$ spinel, and the third layer was identified as an internal oxidation zone (IOZ) next to the metal oxide interface. The IOZ was composed of a mixture of Cr_2O_3 and unreacted iron containing a low amount of chromium [29]. Porous chromium-rich oxide patches were observed inside the IOZ at 550 °C and 600 °C (Fig. 4a and Fig. 4b), as reported in the literature [16,35]. The IOZ was no longer present as a sublayer at higher exposure temperatures starting at 650 °C. Instead of an IOZ, a continuous $(Fe,Cr)_3O_4$ layer encapsulated by a continuous Cr_2O_3 band at the metal oxide interface was present in the form of internally grown oxides. Thus, oxide scales above 600 °C on non-pre-oxidized samples were, an outward grown Fe_2O_3 layer, an inward grown $(Fe,Cr)_3O_4$ layer below the Fe_2O_3 layer, and a continuous Cr_2O_3 band at the metal oxide interface that encapsulated the $(Fe,Cr)_3O_4$ layer.

The effect of temperature on the thickness of these layers showed that the thickness of the Fe_2O_3 layer at 550 °C was 13 μm ± 1 μm (Fig. 4a), whereas at 800 °C, it was 8 μm ± 1 μm (Fig. 4e), indicating an inverse temperature relationship. The same behavior was observed for the $(Fe,Cr)_3O_4$ layer, while the thickness of the Cr_2O_3 band became thicker at elevated temperatures in line with the EDX mapping, (Fig. 5c, d, e).

Fig. 6 shows the cross-sectional SEM micrographs of the air side of the pre-oxidized samples exposed under dual atmosphere conditions, and Fig. 7 shows the EDX mappings obtained from the same cross-sections. Compared to the cross-sections obtained in Fig. 4 where only a non-protective oxide scale was present, the ones in Fig. 6 contain areas with both protective and non-protective oxide scales depending on the exposure temperature. The protective oxide scales had a double-layered structure typically observed in Mn-containing chromia formers. This double-layered structure consisted of an outer $(Cr,Mn)_3O_4$ layer and a Cr_2O_3 layer beneath. Again, the cross-section of samples exposed at 500 °C were not prepared since they exhibited only thin and protective oxide scales. At 550 °C, non-protective oxide nodules and a remaining protective oxide scale were observed together in the cross-section (Fig. 6a). Non-protective oxide scales were composed of an outwards grown Fe_2O_3 scale on top, inwards grown $(Fe,Cr)_3O_4$ below the Fe_2O_3 layer, and an IOZ containing Cr_2O_3 oxide patches below the $(Fe,Cr)_3O_4$ layer towards the metal. At 600 °C (Fig. 6b), only a non-protective oxide scale was detected in the cross-section since this sample was completely covered with a non-protective-oxide scale (Fig. 1, Fig. 3c). At 650 °C and 700 °C, non-protective oxide nodules and a protective oxide scale coexisted together in the cross-section. At this temperature range, the IOZ transformed into $(Fe,Cr)_3O_4$, while the Cr_2O_3 band became a continuous and thick layer. However, newly progressed small IOZs were detected below the Cr_2O_3 band in localized regions. At 800 °C, only a protective oxide scale was observed at the cross-section, pointing out completely protective behavior (Fig. 6g).

Fig. 8 illustrates the cross-sections of pre-oxidized samples exposed at 800 °C under dual or single atmosphere conditions. The spot EDX analysis and scale thickness values are included in order to compare the compositions of the oxide scales. According to Fig. 8, protective double oxide layers composed of $(Cr,Mn)_3O_4$ on top of Cr_2O_3 existed in both cases with a small difference in thickness. The point EDX analysis showed that the composition of the oxide layer on pre-oxidized samples was almost identical regardless if the samples were exposed to single or dual atmosphere at 800 °C and both scales contained less than 1 at% Fe.

4. Discussion

This study investigated the effect of temperature and pre-oxidation on the dual atmosphere effect by exposing 0.2 mm thick non-pre-oxidized and 20 min pre-oxidized AISI 441 steel to temperatures ranging from 500 °C to 800 °C for 336 h under dual and single atmosphere conditions. All samples exposed to the single atmosphere formed protective oxide scales, irrespective of temperature or pre-oxidation condition. The situation was very different under dual atmosphere conditions. Non-pre-oxidized samples exposed to dual atmosphere conditions were completely covered with a non-protective Fe-based oxide scale, except for the samples exposed at 500 °C. Completely protective behavior was observed at 500 °C. The temperature dependence of the non-pre-oxidized samples was not obvious with visual inspection since all samples were covered with thick non-protective oxide scales. However, a comparison of the thickness values of the oxide scales on cross-sections showed a maximum at 550 °C and 600 °C while gradually better protective behavior was observed above 600 °C. 600 °C was the temperature where the most severe corrosion was found for the pre-oxidized samples. Exposures performed at lower or higher temperatures showed a more protective behavior.

Pre-oxidized samples exhibited a larger surface fraction covered with a protective oxide scale as the temperature increased above 600 °C. In

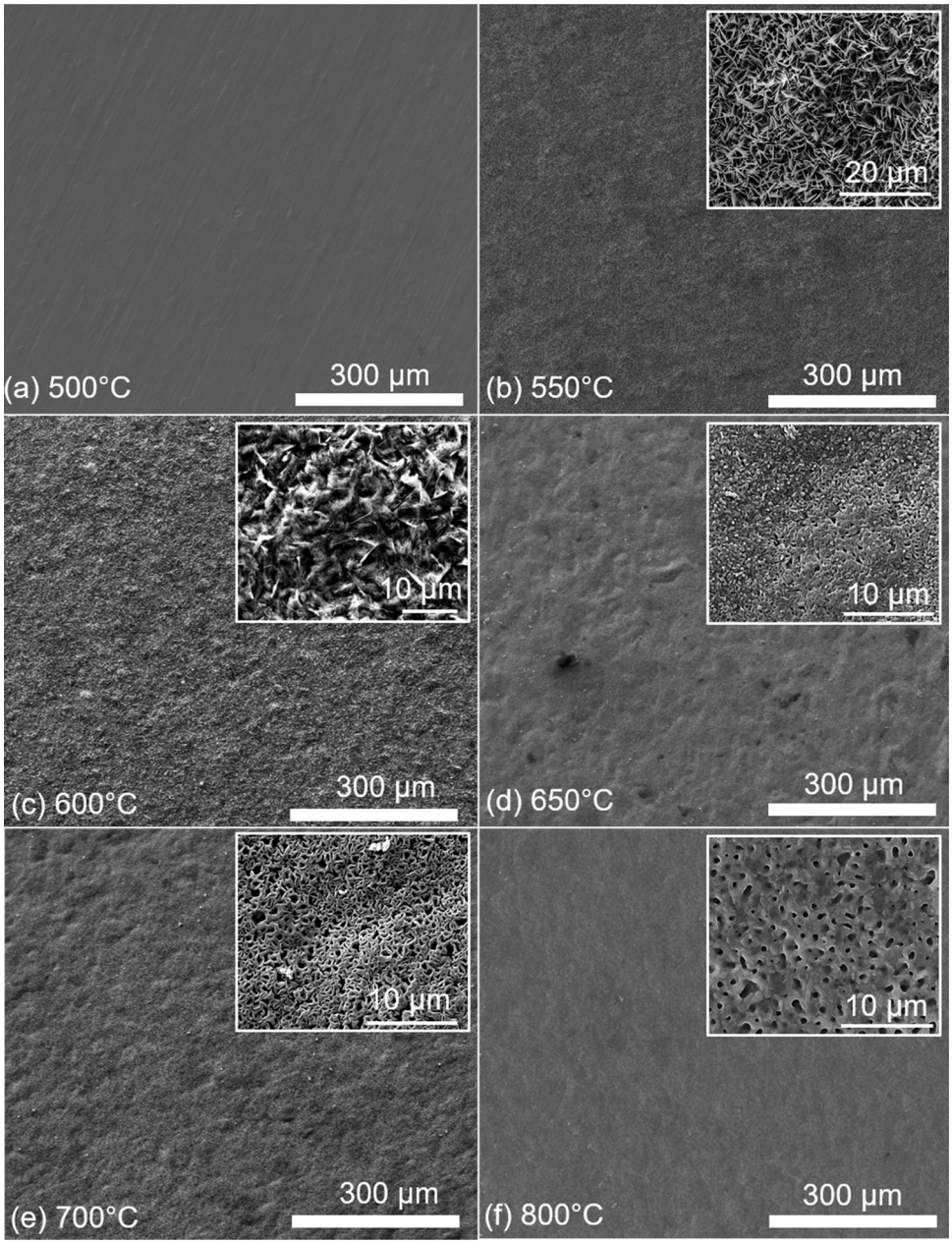

Fig. 2. Plan view SEM images of the non-pre-oxidized samples exposed for 336 h under dual atmosphere conditions at different temperatures; a) 500 °C, b) 550 °C, c) 600 °C, d) 650 °C, e) 700 °C, and f) 800 °C.

fact, pre-oxidized samples exhibited only protective Cr-rich oxide scales at 800 °C, and no apparent difference between the oxide scales under single and dual atmosphere conditions was observed.

The large difference in oxidation behavior observed for some of the samples between single and dual atmosphere exposures was due to the competition between a slow-growing, protective Cr-rich oxide scale or a poorly protective much faster growing Fe-rich oxide scale, obviously related to hydrogen. This competition has been described in the classical theories of internal [36] and selective [37] oxidation by Wagner. The formation and maintenance of protective external oxide scales requires that two Wagnerian criteria are satisfied. The first one, given in Eq. (1), is relevant for the non-pre-oxidized samples, and states that the Cr concentration of the alloy must exceed the critical Cr concentration ($N_{Cr}^{crit,1}$) necessary to overcome the inward oxygen ingress by outward Cr flux to prevent internal oxidation.

$$N_{Cr}^{crit,1} > \left[\frac{\pi g^*}{3}\frac{\overline{V}_m}{\overline{V}ox}\frac{N_O^{(s)} D_O}{\tilde{D}_{Cr}}\right]^{\frac{1}{2}} \quad (1)$$

where $N_O^{(s)}$ is the oxygen solubility in the alloy in terms of mole-fraction, D_O is the diffusivity of oxygen in m^2s^{-1}, $\tilde{D}_{Cr}$ is the chemical diffusivity of chromium in m^2s^{-1}, $\overline{V}_m$ and $\overline{V}ox$ are the molar volumes of the alloy and oxide in $m^3\,mol^{-1}$, respectively. The internal oxide in the Fe-Cr system is generally assumed to be chromia, thus, the $\overline{V}_m$ and $\overline{V}ox$ are 7 and 15 $cm^3\,mol^{-1}$, respectively. The factor g^* has been approximated by Rapp [38] as 0.3. It should be noted that Eq. 1 was originally derived under conditions where only Cr forms a thermodynamically stable oxide [36]. However, Gesmundo and Viani [39] have shown in their theoretical analysis that the external oxidation of Fe increases the critical solute concentration, $N_{Cr}^{crit,1}$. This is important as, in addition to Cr, Fe also oxidizes in most oxidation scenarios, including dual atmosphere

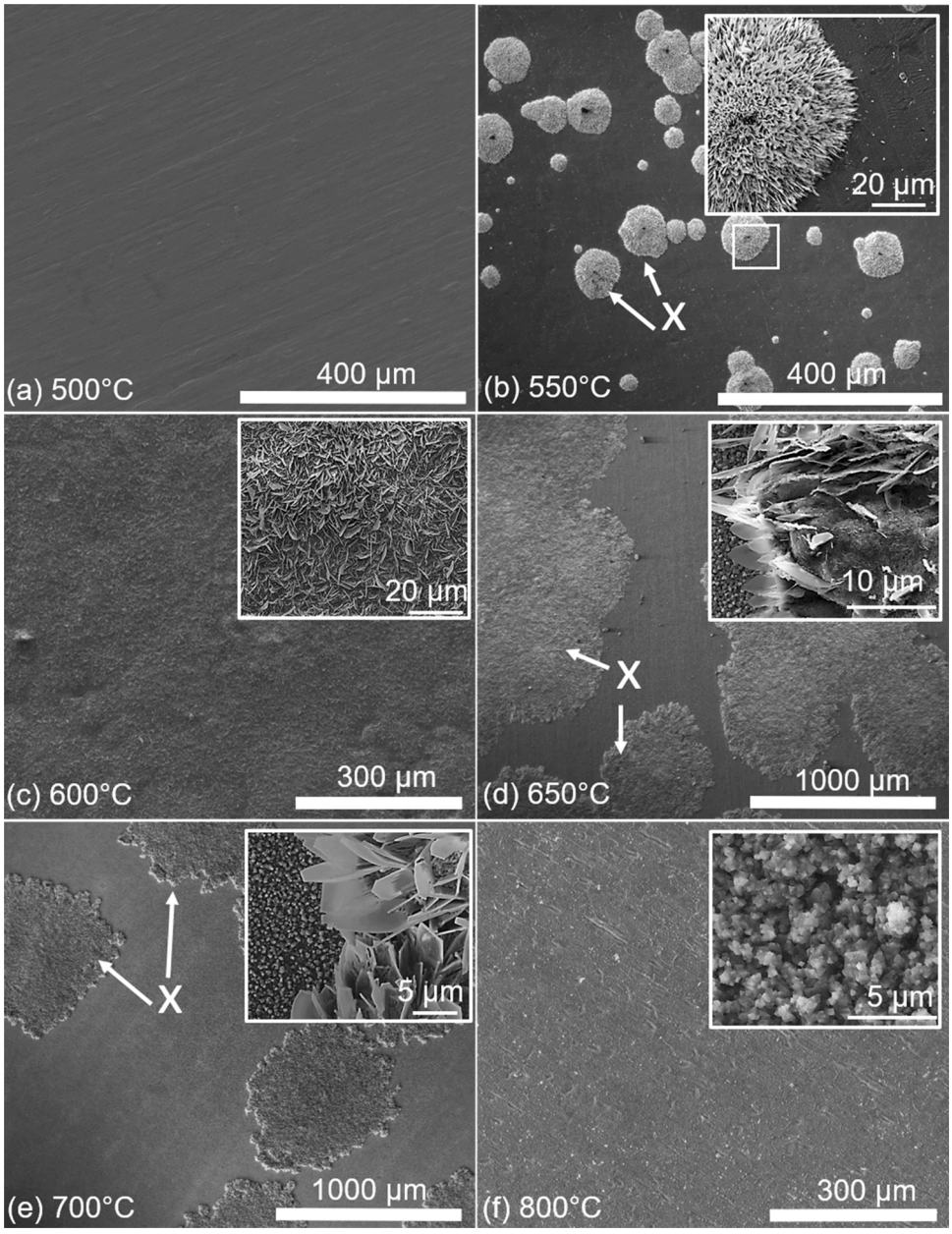

Fig. 3. Plan view SEM images of the pre-oxidized samples exposed for 336 h under dual atmosphere conditions at different temperatures; a) 500 °C, b) 550 °C, c) 600 °C, d) 650 °C, e) 700 °C, and f) 800 °C. X points out the non-protective oxide, other regions are protective.

oxidation. However, Wagner's model is commonly used to simplify the calculations.

The second criterion was derived from the Wagnerian depletion model and predicts the minimum Cr concentration, $N_{Cr}^{crit,2}$, in the alloy to sustain the protective Cr_2O_3 scale once an external oxide layer has been formed. The second criterion can be expressed as

$$N_{Cr}^{crit,2} > \frac{\overline{V}_m}{32\nu}\left(\frac{k_p}{\tilde{D}_{Cr}}\right)^{\frac{1}{2}} \quad (2)$$

where k_p is the parabolic rate constant for the growth of the external oxide scale in m^2s^{-1}.This criterion is relevant for pre-oxidized specimens. Values of $N_{Cr}^{crit,1}$ and $N_{Cr}^{crit,2}$ for the Fe-Cr binary system have been calculated in a number of studies [40,41] and suggest that only 7 wt% Cr is sufficient to form and sustain a protective Cr_2O_3 scale in the temperature range of 500−800 °C. In these calculations, $N_{Cr}^{crit,1}$ increases with temperature, while $N_{Cr}^{crit,2}$ diminishes. The data for the calculations in [40] originate from various sources: the data for $N_O^{(s)}D_O$ were taken from [42], the values for $\tilde{D}_{Cr}$ and k_p were extrapolated from the data in [43].

The $N_O^{(s)}D_O$ data obtained by Swisher et al. [42] were obtained at temperatures between 881 °C and 1350 °C for δ-iron and were further extrapolated for α-iron. However, Takada et al. directly measured the $N_O^{(s)}D_O$ values of ferritic Fe–Al [44] and Fe–Si [45] alloys between 750 °C and 900 °C. Therefore, the $N_O^{(s)}D_O$ values from Takada et al. were used in this study, because the temperature range was more relevant for the SOFC applications and the oxygen permeability data were directly measured on α-iron, which makes the values more reliable. In addition, the $N_O^{(s)}D_O$ values of Takada et al. are in excellent agreement with recent studies [46,47] arriving at the same activation energy value for oxygen permeation in α-iron, i.e. 200 kJ mol^{-1}.

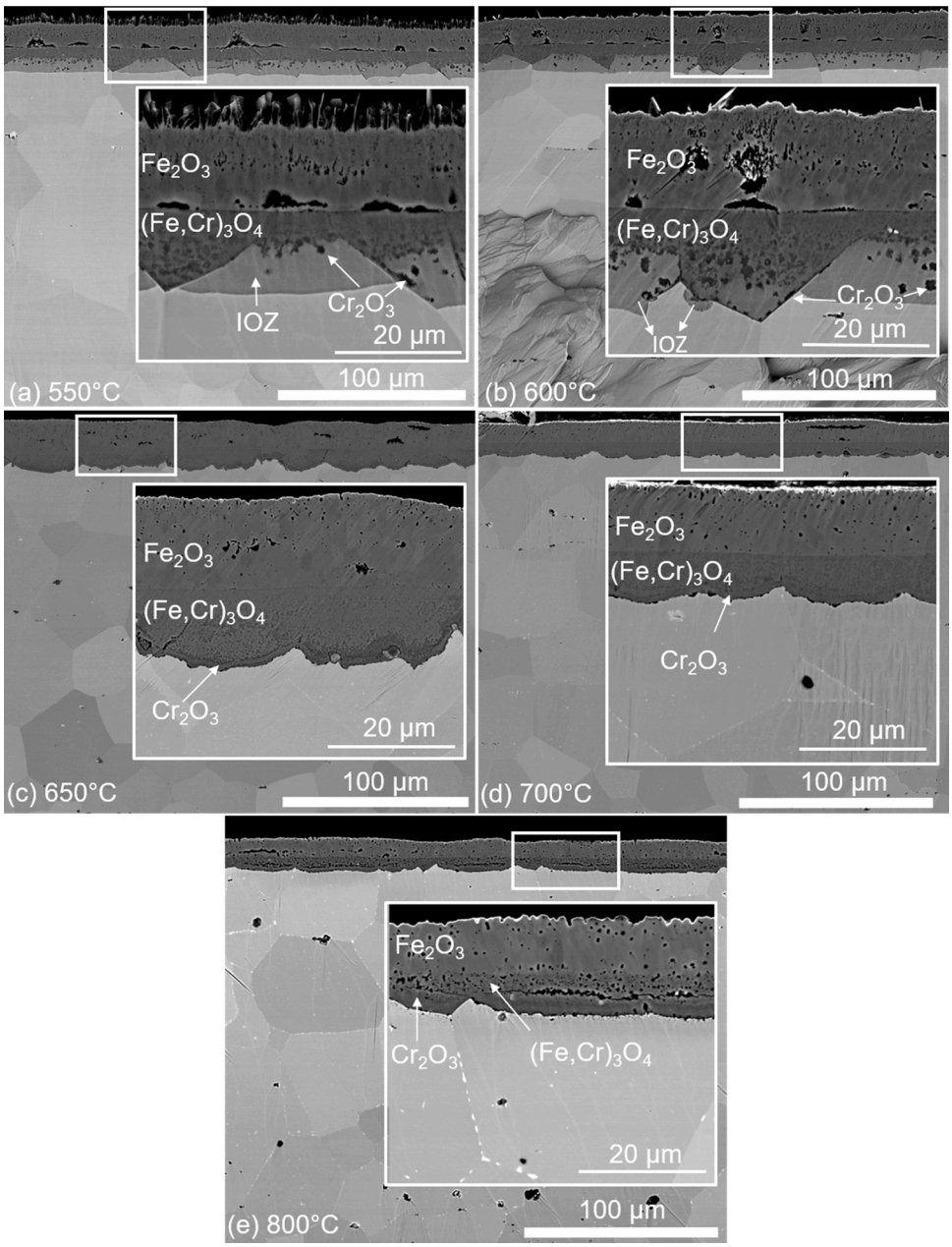

Fig. 4. Cross-sectional SEM images of the non-pre-oxidized samples after 336 h dual atmosphere exposure at different temperatures.

The chromium inter-diffusion coefficients in [43] were calculated from the Cr depletion profiles in Fe-Cr specimens oxidized at 900−1200 °C. The Cr diffusivities were extrapolated to lower temperatures, and the activation energy for Cr diffusion was estimated as 179 kJ mol^{-1}. The lower E_A for Cr diffusion with respect to $N_O^{(s)} D_O$ thus explains the positive temperature dependence of $N_{Cr}^{crit,1}$ calculated in several studies [40,41].

However, the abundant literature data on Cr diffusion in iron and Fe-Cr alloys suggest a higher activation energy for Cr diffusion. The values of 267 [48] and 258−279 kJ mol^{-1} [49] have been reported in tracer diffusion studies performed on single crystals, a lower activation energy of 210 kJ mol^{-1} was determined from diffusion couple experiments on polycrystalline AISI446 (grain size: 30 µm) and mild steel [50]. The Cr diffusion data from all available sources were critically reviewed in the latter publication, suggesting 210 kJ mol^{-1} as the most realistic value for the E_A of Cr diffusion [50].

The tracer Cr diffusivities from [48,49] dramatically overestimate $N_{Cr}^{crit,2}$ and predict non-protective behavior throughout the entire temperature range, which was clearly not observed under single atmosphere conditions. The Cr diffusion in steel is obviously dominated by the grain boundary (GB) contribution below 700 °C, which is hard to assess quantitatively due to a lack of Cr GB diffusion data on high-alloyed steels. However, one might estimate the order of magnitude of the GB term using the available data for iron GB diffusion [51] and the expression

$$D_{eff} = D_L + \frac{1}{2d} S\delta D_{GB} \tag{3}$$

where D_L is the lattice diffusivity in m^{2}s^{-1}, D_{GB} is the grain boundary diffusivity in m^{2}s^{-1}, δ is the grain boundary width in m, and d is the grain size in m. Segregation factor S is neglected to simplify the problem. The δ parameter is universally taken as 0.5 nm. Eq. (3) reveals that the effective diffusion coefficient at 600 °C is approximately two orders of magnitude higher than the lattice diffusion coefficient. The contribution of GB diffusion gradually diminished with increasing temperature. The

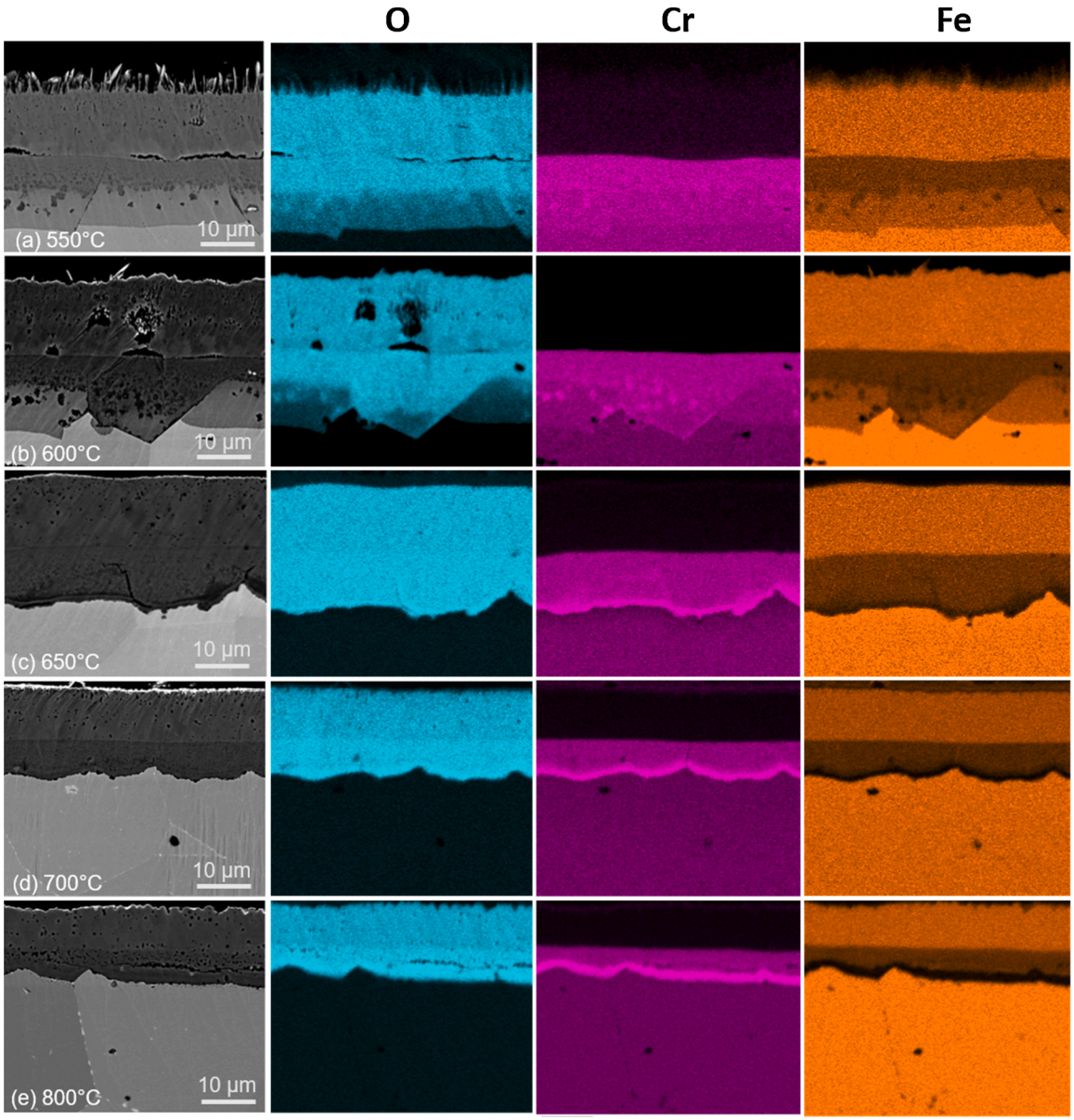

Fig. 5. SEM-EDX mapping of cross-sections of the non-pre-oxidized samples exposed under dual atmosphere conditions for 336 h at different temperatures; a) 550 °C, b) 600 °C, c) 650 °C, d) 700 °C, and e) 800 °C.

Cr diffusion data obtained for polycrystals were much closer to the estimations by Eq. (3) in the temperature range of interest, 550−800 °C, and should therefore be a better choice for Eq. (2). Consequently, the data of Williams et al. [50] will be used in this study instead of the data of Whittle et al. [43], which underestimates the activation energy for Cr diffusion. Calculated parameters are given in Table 2.

The temperature dependence trend for $N_{Cr}^{crit,1}$ reverses (Table 2) with the higher activation energy for Cr diffusion, i.e. less Cr is required at a higher temperature to initially form a protective oxide scale. The latter was clearly observed at 500−800 °C (Figs. 4 and 5) in non-pre-oxidized specimens. An IOZ beneath the spinel layer, i.e. the finely dispersed Cr_2O_3 particles in the iron matrix, was clearly observed at 550 and 600 °C (Fig. 4a, b), while it transformed into a $(Fe,Cr)_3O_4$ spinel layer with a Cr_2O_3 sub-layer (Fig. 4c–e) with increasing temperature. The overall thickness of the outer and inner layers was found to tend to diminish with increasing temperature, suggesting that the outward Cr transport was dominant at 700−800 °C, indicating more protective behavior.

Once a scale has been formed or pre-formed, Wagner's second criterion must be analyzed to evaluate the sustainability of the chromia growth. Oxidation kinetics were taken from FalkWindisch et al. [52]. Data were obtained for a Fe-22Cr steel (Sanergy HT) and were additionally corrected for Cr evaporation to yield the gross oxide growth rate. Almost identical oxidation kinetics were recently obtained for an AISI 441 FSS by Reddy et al. [53].

This data set predicts a slight variation of $N_{Cr}^{crit,2}$ from 1 to 2 wt% (Table 2), which agrees well with experimental observations for chromia-forming ferritic materials in air, since virtually flat Cr depletion profiles were obtained through the oxidation of ferritic steels [54–56]. Wagner originally derived the second criterion under conditions where only the more reactive element, Cr in this case, could oxidize and estimated the Cr concentration at the metal/oxide interface as zero to maximize the flux. However, aforementioned studies have also shown that FSS had already failed when it was depleted to 8−10 wt% Cr. Therefore, the latter value is a reasonable estimate of a correction factor to add to the data in Table 2. The weak temperature dependence of $N_{Cr}^{crit,2}$ can be understood by comparing the activation energies of oxide formation and Cr diffusion: the E_A for oxide growth is 261 kJ mol^{-1} [11],

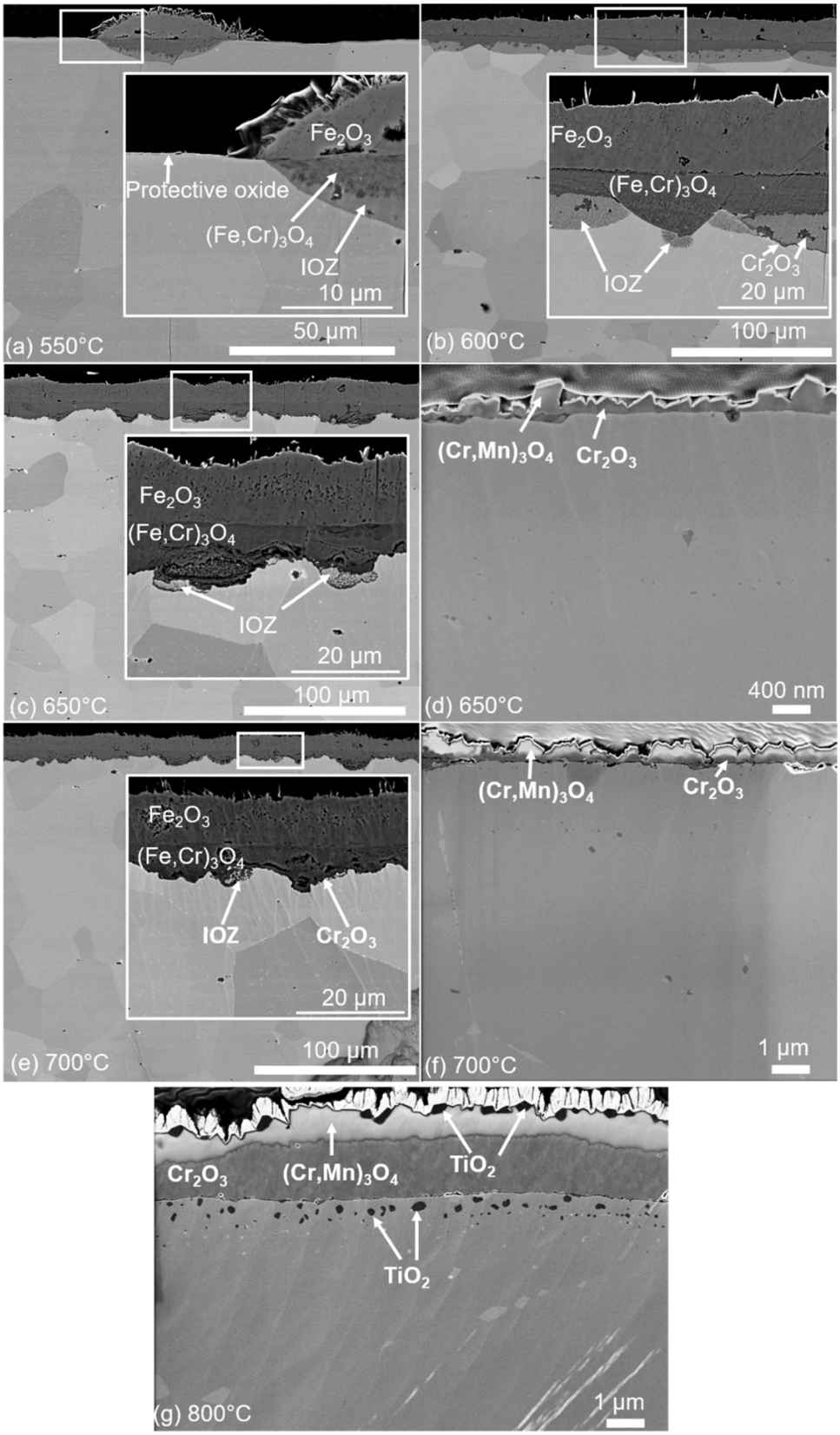

Fig. 6. SEM cross-section images of the pre-oxidized samples after exposure at different temperatures under dual atmosphere conditions for 336 h: a) 550 °C, b) 600 °C, c) 650 °C non protective, d) 650 °C protective, e) 700 °C non protective, f) 700 °C protective, and g) 800 °C.

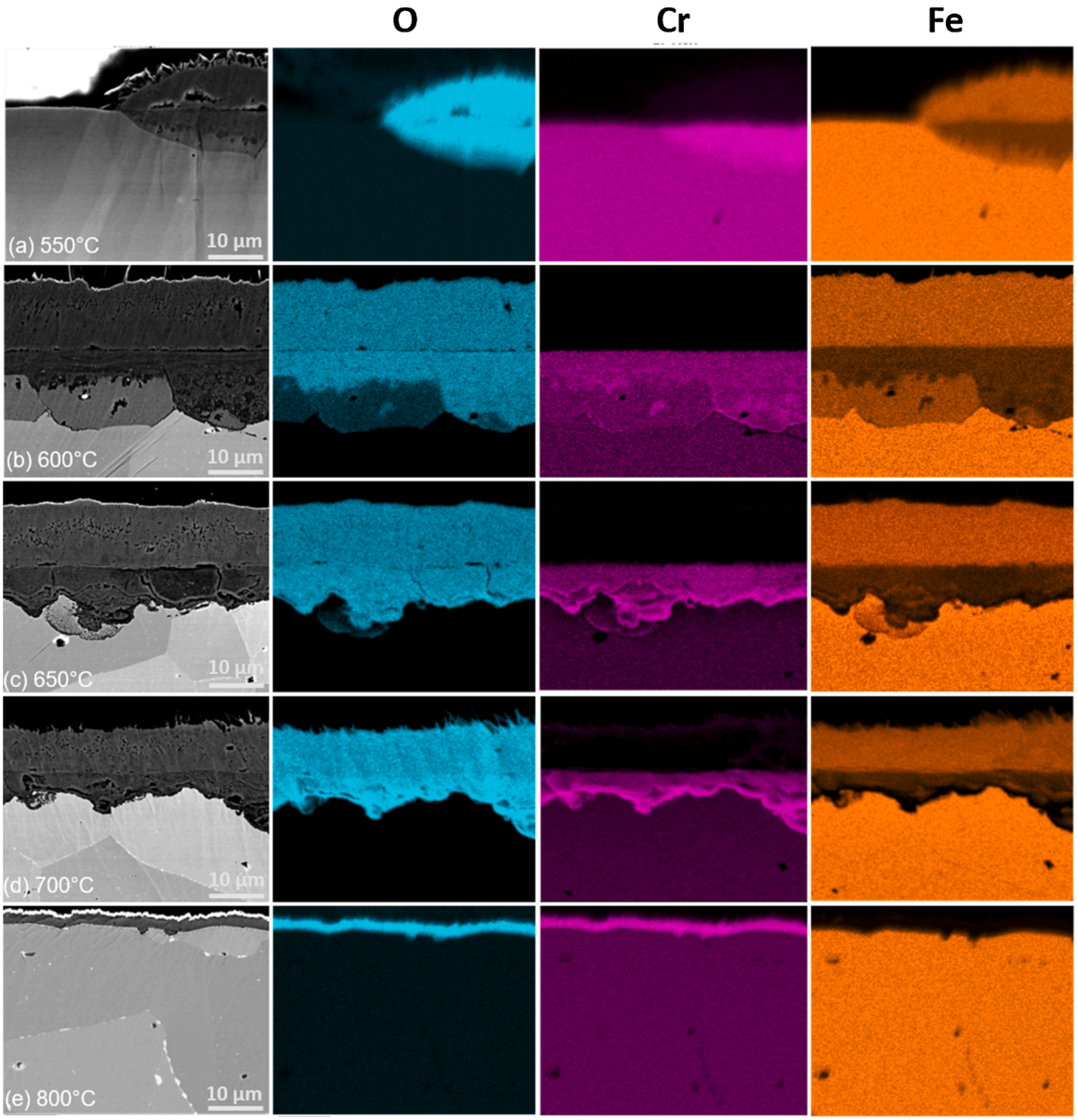

Fig. 7. SEM-EDX mapping of cross-section of pre-oxidized samples exposed under dual atmosphere conditions for 336 h at different temperatures: a) 550 °C, b) 600 °C, c) 650 °C, d)700 °C, and e) 800 °C.

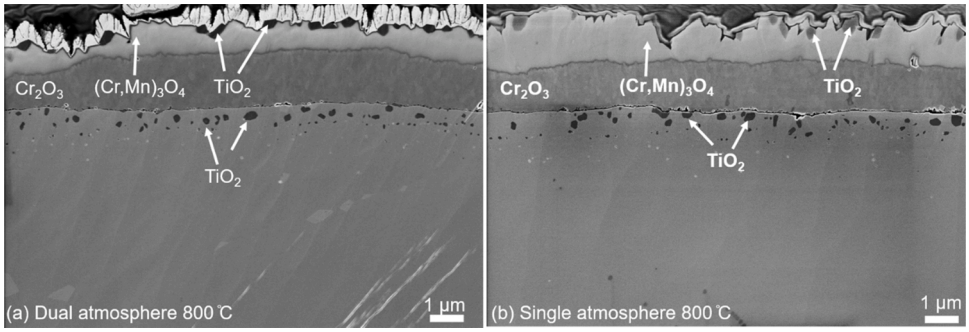

Fig. 8. SEM images of cross-sections of pre-oxidized samples exposed at 800 °C for 336 h under: a) dual atmosphere conditions and b) single atmosphere conditions.

which is close to the E_A for Cr diffusion, 210 kJ mol^{-1}, and agrees well with the vast data on chromia scales on pure Cr and on alloys [57–61].

Considering the dual atmosphere effect in light of Wagner's model, hydrogen arriving from the fuel side may affect three key parameters in Eqs. (1) and (2): i) oxygen permeability $N_O^{(s)} D_O$, ii) chromia growth rate (k_p), and iii) Cr diffusion $\tilde{D}_{Cr}$. Before evaluating these parameters, it should be mentioned that the activation energies for oxygen permeation

Table 2
Literature values used in the calculation of $N_{Cr}^{crit,1}$ and $N_{Cr}^{crit,2}$ for Fe-Cr alloys with Eq. (1) and Eq. (2), respectively.

T (°C)	$N_O^{(s)}$	D_O (m^2s^{-1})	$\tilde{D}_{Cr}$ (m^2s^{-1})	k_p (m^2s^{-1})	$N_{Cr}^{crit,1}$	$N_{Cr}^{crit,2}$
500	3.6×10^{-8}	2.9×10^{-13}	9.7×10^{-20}	1.2×10^{-23}	0.127	0.003
550	9.5×10^{-8}	6.5×10^{-13}	7.0×10^{-19}	1.4×10^{-22}	0.116	0.004
600	2.3×10^{-7}	1.3×10^{-12}	4.1×10^{-18}	1.3×10^{-21}	0.106	0.005
650	4.9×10^{-7}	2.5×10^{-12}	1.9×10^{-17}	9.0×10^{-21}	0.099	0.006
700	9.9×10^{-7}	4.5×10^{-12}	8.0×10^{-17}	5.2×10^{-20}	0.092	0.007
800	3.3×10^{-6}	1.2×10^{-11}	9.0×10^{-16}	1.0×10^{-18}	0.082	0.009
900	8.9×10^{-6}	2.7×10^{-11}	6.7×10^{-15}	1.3×10^{-17}	0.074	0.011

(200 kJ mol^{-1}), Cr diffusion (210 kJ mol^{-1}), and oxidation (260 kJ mol^{-1}) are very close. Therefore, there should be no extreme temperature dependence effects with respect to these parameters. The chromium and oxygen fluxes match in a broad temperature interval. Apparently, hydrogen disrupts this equilibrium, affecting one of these parameters.

No unanimous opinion on the role of hydrogen on internal oxidation and, hence, its effect on oxygen permeability was found in the literature. Water vapor as an oxidant, however, is well known to induce the breakaway oxidation of ferritic steels [62,63] and to lead to internal oxidation. Essuman et al. [63] have suggested that hydrogen interstitials expand the iron lattice so that the diffusivity of oxygen increases. However, there is also abundant experimental evidence of the commensurate internal oxidation of Al or Ti underneath an external Cr_2O_3 scale in air and H_2-H_2O gas mixtures [56,64–66], especially in dual atmosphere exposures [18]. This strongly suggests that no such effect exists.

Oxygen permeability must be increased at least by a factor of 3 or 4 to shift $N_{Cr}^{crit,1}$ to the level of 0.190 (18 wt%) at 600 °C and 700 °C, respectively, thereby, rendering the alloy unable to passivate even in an air-only atmosphere. In practical terms, such an increase in $N_O^{(s)}D_O$ would result in doubling the IOZ thickness, which would be clearly visible in the abovementioned works, however, this is not the case [56, 64,66]. Instead the reported variations of $N_O^{(s)}D_O$ in dry and wet gases often fall within the margin of experimental error.

In their pioneering work Yang et al. [15] have explained the dual atmosphere in terms of hydrogen doping the oxide scale, leading to faster oxide scale growth. Skilbred et al. [18] and Rufner et al. [25] have put forth similar arguments. The effect of hydrogen on the scaling rate under dual atmosphere conditions can be estimated from the experiments of Skilbred et al. [18] and Alnegren et al. [30]. No significant increase in the scale thickness between dual and single conditions was observed after 500 h at 800 °C. Following the same approach as above, k_p can also be varied in Eq. (2) to arrive at an even more surprising finding: if k_p is increased by an order of magnitude, $N_{Cr}^{crit,2}$ remains below 0.180 between 500 °C and 800 °C. This result is attributed to rapid diffusion in the BCC lattice. Thus, the dual atmosphere effect can hardly be explained by the acceleration of the oxidation rate.

Cr diffusion thus remains the ultimate parameter to analyze in Eq. (1) and Eq. (2). The effect of hydrogen on Cr diffusion in Fe–Cr alloys was found to be negligible in the study by Ani et al. [47]. However, the diffusion couple experiments carried out at 800 °C on coarse-grained materials only demonstrated that the lattice diffusion of Cr is not affected by hydrogen. To the best of the authors' knowledge, there is no experimental data in the literature on the effect of hydrogen on GB transport.The GB effect can still be analyzed using Eq. (1) and Eq. (2). For the non-pre-oxidized specimens (criterion 1), $\tilde{D}_{Cr}$ needs to be decreased only by a factor of 5 to result in non-protective behavior according to Eq. (1). For the pre-oxidized specimens (criterion 2), $\tilde{D}_{Cr}$ needs to be decreased by approximately two orders of magnitude in order to predict non-protective behavior.

Given the temperature dependence of the dual atmosphere effect in the present work and previous studies, it is reasonable to assume that the mechanism of hydrogen effect on chromia scale protectiveness might be related to the mitigation of the Cr transport at GBs. Consequently, this effect would be expected to be more pronounced at lower temperatures. Apart from the greater sensitivity of criterion 1, to a change in $\tilde{D}_{Cr}$, it is also expected that the higher amount of hydrogen permeating the steel exacerbates the negative effect of hydrogen on non-pre-oxidized samples. Kurokawa et al. [67] have studied this hydrogen permeation through bare and oxidized AISI 430 steel and found 3–4 orders of magnitude lower hydrogen permeation after an oxide scale had formed [67]. These findings show that Cr_2O_3 is an effective barrier against hydrogen permeation, and they are further corroborated by the works of Amendola et al. [31] and Goebel et al. [20] who have demonstrated the beneficial effects of pre-oxidation under dual atmosphere conditions at 800 °C and 600 °C, respectively.

Although there is no direct experimental evidence for the hypothesis that hydrogen affects D_{GB}, the fact that all other possible factors can be excluded make this hypothesis very plausible. There might be a few possible scenarios of hydrogen effect on Cr transport at GBs such as hydride formation or obstructing chromium diffusion owing to the adsorption of hydrogen on internal surfaces of grain boundaries. However, further studies including isotope exposures with D_2 and D_2O, Cr tracer studies are needed for better understanding the role of hydrogen in Cr transport through Fe–Cr alloys and the dual atmosphere effect in general. In addition, DFT calculations might shed some light on the hydride formation possibility at the grain boundaries.

What cannot be explained by the discussion so far is the trend for a more protective behavior below 600 °C. However, Cr_2O_3 and Fe_2O_3 are fully miscible, and Segerdahl et al. [68] have shown that at lower temperatures more Fe is incorporated into the oxide of 11 wt. % Cr steels. In fact, protective behavior was observed in these experiments at 500 °C despite the oxide being almost pure Fe_2O_3. Visual inspection (Fig. 1) and plan view images (Fig. 2) of non-pre-oxidized samples at 500 °C revealed identical surfaces, which further supports this hypothesis.

Although Alnegren et al. [30] have stated that no dual atmosphere effect was observed at 700 °C and 800 °C, the findings in the present study match well with the data published by those authors [30]. A comparison of the 800 °C sample that was pre-oxidized for 20 min with the sample exposed under single atmosphere conditions revealed only minimal differences (see Fig. 8). The same conclusion was reached by Alnegren et al. [30] after 1000 h exposure under identical conditions with a sample that was pre-oxidized for 3 h. It is only under the much harsher non-pre-oxidized conditions examined in the present work that a dual atmosphere effect was observed at 800 °C. The differences observed at 700 °C can be explained by the work of *Goebel* et al. [20]; the onset of non-protective oxide scale formation correlates directly with the length of pre-oxidation. Thus, the 3 h pre-oxidation performed by Alnegren et al. kept the oxide protective for > 1000 h at 700 °C. However, with a pre-oxidation of only 20 min, a non-protective oxide scale started to form within the first 336 h of exposure. Many of the discrepancies on the dual atmosphere effect in the literature can be understood by combining the findings by Alnegren et al. [30], Goebel et al. [20], and the present work.

For example, Kurokawa et al. [24] used 2 mm thick steels and exposed the samples for 168 h at 800 °C and used Pyrex rings as a sealing material. Some time is needed to obtain a complete seal with Pyrex. Based on data published by Kurokawa et al. in another study [67] sealing seemed to be complete after 5 ks, which corresponds to 1.4 h. This period probably corresponds to a pre-oxidation step, because during this period air leaks in and hydrogen leaks out. Thus, the fact that no

clear dual atmosphere effect was observed by those authors would be expected, particularly considering the thick steel that was used. A thicker steel would be expected to alleviate the dual atmosphere effect to a certain extent, as has been shown by Goebel et al. [22]. Stygar et al. [28] used a setup similar to Kurokawa et al. and did not observe any dual atmosphere effect, probably for the same reason. The most severe dual atmosphere effects have been reported by the groups at Chalmers [20,29,30] and Montana State University [22,25,31,33]. Both groups have used a similar design that relies on clamping the sample with a gasket, where no heat treatment is required. Thus, if no deliberate pre-oxidation step is included, a non-pre-oxidized metal surface will be exposed to dual atmosphere conditions. Skilbred et al. [18,19] have used a similar clamping setup and reported only a mild dual atmosphere effect. This can probably be explained by the high temperature interval (800−900 °C) in that study in combination with a higher alloyed (22 wt% Cr) steel, which also contained reactive element additions (Sanergy HT).

5. Conclusion

In this study, exposures under dual and single atmosphere conditions were performed on AISI 441 steel with or without pre-oxidation in a wide temperature range (500 °C–800 °C) for 336 h. All samples exposed to a single atmosphere formed protective oxide scales. Both non-pre-oxidized and pre-oxidized samples were protective at 500 °C. The non-pre-oxidized samples exhibited breakaway corrosion at all other temperatures due to the easy ingress of hydrogen from the fuel side. The most severe corrosion for the pre-oxidized samples was observed at 600 °C. The surface fraction of protective oxide increased if the temperature was decreased or increased from 600 °C. The obtained results were analyzed with Wagner's oxidation criteria. In light of this analysis, a new hypothesis concluded that hydrogen decreased the grain boundary contribution of Cr diffusion, which promoted the formation of the non-protective Fe-based oxide. Findings demonstrate the beneficial effect of pre-oxidation and allow for an explanation of the numerous discrepancies in the literature on the existence and magnitude of the dual atmosphere effect.

Data availability

The raw/processed data required to reproduce these findings will be made available on request.

CRediT authorship contribution statement

Kerem O. Gunduz: Conceptualization, Investigation, Writing - original draft, Writing - review & editing. **Anton Chyrkin:** Conceptualization, Formal analysis, Writing - review & editing. **Claudia Goebel:** Conceptualization, Investigation, Writing - review & editing. **Lukas Hansen:** Investigation. **Oscar Hjorth:** Investigation. **Jan-Erik Svensson:** Writing - review & editing, Supervision, Funding acquisition. **Jan Froitzheim:** Conceptualization, Writing - review & editing, Funding acquisition, Supervision, Project administration.

Declaration of Competing Interest

The authors declare that they have no known competing financial interests or personal relationships that could have appeared to influence the work reported in this paper.

Acknowledgements

The authors are grateful for funding by the Swedish Energy Agency (grant 2015-009652), the FFI program, as well as the Swedish High Temperature Corrosion Centre. This work was performed in part at the Chalmers Material Analysis Laboratory, CMAL. One of the authors of this work, Kerem Ozgur Gunduz, acknowledges financial support of Scientific and Technological Research Council of Turkey through the program number TUBITAK-2219.

References

[1] E.D. Wachsman, K.T. Lee, Lowering the temperature of solid oxide fuel cells, Science 334 (2011) 935–939.
[2] R.P. O'Hayre, Fuel Cell Fundamentals, John Wiley & Sons, Hoboken, N.J, 2006.
[3] J.W. Wu, X.B. Liu, Recent development of SOFC metallic interconnect, J. Mater. Sci. Technol. 26 (2010) 293–305.
[4] W.Z. Zhu, S.C. Deevi, Development of interconnect materials for solid oxide fuel cells, Mat Sci Eng a-Struct 348 (2003) 227–243.
[5] J.C.W. Mah, A. Muchtar, M.R. Somalu, M.J. Ghazali, Metallic interconnects for solid oxide fuel cell: a review on protective coating and deposition techniques, Int. J. Hydrogen Energ. 42 (2017) 9219–9229.
[6] J.W. Fergus, Metallic interconnects for solid oxide fuel cells, Mater. Sci. Eng. A-Struct. 397 (2005) 271–283.
[7] P.D. Jablonski, C.J. Cowen, J.S. Sears, Exploration of alloy 441 chemistry for solid oxide fuel cell interconnect application, J. Power Sources 195 (2010) 813–820.
[8] J. Froitzheim, E. Larsson, L.G. Johansson, J.E. Svensson, Cr evaporation of metallic interconnects: a novel method for quantification, Solid Oxide Fuel Cells 11 (Sofc-Xi) 25 (2009) 1423–1428.
[9] J. Froitzheim, H. Ravash, E. Larsson, L.G. Johansson, J.E. Svensson, Investigation of chromium volatilization from FeCr interconnects by a denuder technique, J. Electrochem. Soc. 157 (2010) B1295–B1300.
[10] C. Goebel, R. Berger, C. Bernuy-Lopez, J. Westlinder, J.E. Svensson, J. Froitzheim, Long-term (4 year) degradation behavior of coated stainless steel 441 used for solid oxide fuel cell interconnect applications, J. Power Sources 449 (2020).
[11] H.F. Windisch, J. Froitzheim, J.E. Svensson, Influence of chromium evaporation and oxidation on interconnect steels at 650-850 degrees C, Solid Oxide Fuel Cells 13 (Sofc-Xiii) 57 (2013) 2225–2233.
[12] C. Goebel, A.G. Fefekos, J.E. Svensson, J. Froitzheim, Does the conductivity of interconnect coatings matter for solid oxide fuel cell applications? J. Power Sources 383 (2018) 110–114.
[13] H. Falk-Windisch, J. Claquesin, M. Sattari, J.E. Svensson, J. Froitzheim, Co- and Ce/Co-coated ferritic stainless steel as interconnect material for intermediate temperature solid oxide fuel cells, J. Power Sources 343 (2017) 1–10.
[14] J.G. Grolig, J. Froitzheim, J.E. Svensson, Effect of cerium on the electrical properties of a cobalt conversion coating for solid oxide fuel cell interconnects - a study using impedance spectroscopy, Electrochim. Acta 184 (2015) 301–307.
[15] Z.G. Yang, M.S. Walker, P. Singh, J.W. Stevenson, Anomalous corrosion behavior of stainless steels under SOFC interconnect exposure conditions, Electrochem. Solid State 6 (2003) B35–B37.
[16] M.R. Ardigo, I. Popa, L. Combemale, S. Chevalier, F. Herbst, P. Girardon, Dual atmosphere study of the K41X stainless steel for interconnect application in high temperature water vapour electrolysis, Int. J. Hydrogen Energ. 40 (2015) 5305–5312.
[17] G.R. Holcomb, M. Ziomek-Moroz, S.D. Cramer, B.S. Covino, S.J. Bullard, Dual-environment effects on the oxidation of metallic interconnects, J. Mater. Eng. Perform. 15 (2006) 404–409.
[18] A.W.B. Skilbred, R. Haugsrud, The effect of dual atmosphere conditions on the corrosion of Sandvik Sanergy HT, Int. J. Hydrogen Energ. 37 (2012) 8095–8101.
[19] A.W.B. Skilbred, R. Haugsrud, The effect of water vapour on the corrosion of sandvik sanergy HT under dual atmosphere conditions, Oxid. Met. 79 (2013) 639–654.
[20] C. Goebel, P. Alnegren, R. Faust, J.E. Svensson, J. Froitzheim, The effect of pre-oxidation parameters on the corrosion behavior of AISI 441 in dual atmosphere, Int. J. Hydrogen Energ. 43 (2018) 14665–14674.
[21] Z.G. Yang, G.G. Xia, M.S. Walker, C.M. Wang, J.W. Stevenson, P. Singh, High temperature oxidation/corrosion behavior of metals and alloys under a hydrogen gradient, Int. J. Hydrogen Energ. 32 (2007) 3770–3777.
[22] C. Goebel, C. Bo, J.-E. Svensson, J. Froitzheim, The influence of different factors on the dual atmosphere effect observed for AISI 441 interconnects used in solid oxide fuel cells, ECS Trans. 91 (2019) 2261–2266.
[23] J. Li, D. Yan, Y.P. Gong, Y.X. Jiang, J. Li, J. Pu, B. Chi, L. Jian, Investigation of anomalous oxidation behavior of SUS430 alloy in solid oxide fuel cell dual atmosphere, J. Electrochem. Soc. 164 (2017) C945–C951.
[24] H. Kurokawa, K. Kawamura, T. Maruyama, Oxidation behavior of Fe-16Cr alloy interconnect for SOFC under hydrogen potential gradient, Solid State Ion 168 (2004) 13–21.
[25] J. Rufner, P. Gannon, P. White, M. Deibert, S. Teintze, R. Smith, H. Chen, Oxidation behavior of stainless steel 430 and 441 at 800 degrees C in single (air/air) and dual atmosphere (air/hydrogen) exposures, Int. J. Hydrogen Energ. 33 (2008) 1392–1398.
[26] Y. Zhao, J.W. Fergus, Oxidation behavior of stainless steel 441 and 430 in dual atmosphere - effects of alloy grain boundaries, in: High Temperature Corrosion and Materials Chemistry 9 - a Symposium in Honor of Professor Robert A. Rapp, 41, 2012, pp. 147–154.
[27] Y. Zhao, J.W. Fergus, Oxidation of alloys 430 and 441 in SOFC dual atmospheres: effects of flow rate and humidity, J. Electrochem. Soc. 159 (2012) C109–C113.
[28] M. Stygar, T. Brylewski, A. Kruk, K. Przybylski, Oxidation properties of ferritic stainless steel in dual Ar-H-2-H2O/air atmosphere exposure with regard to SOFC interconnect application, Solid State Ion. 262 (2014) 449–453.
[29] P. Alnegren, M. Sattari, J.E. Svensson, J. Froitzheim, Severe dual atmosphere effect at 600 degrees C for stainless steel 441, J. Power Sources 301 (2016) 170–178.

[30] P. Alnegren, M. Sattari, J.E. Svensson, J. Froitzheim, Temperature dependence of corrosion of ferritic stainless steel in dual atmosphere at 600-800 degrees C, J. Power Sources 392 (2018) 129–138.
[31] R. Amendola, P. Gannon, B. Ellingwood, K. Hoyt, P. Piccardo, P. Genocchio, Oxidation behavior of coated and preoxidized ferritic steel in single and dual atmosphere exposures at 800 degrees C, Surf. Coat. Technol. 206 (2012) 2173–2180.
[32] M. Stygar, K. Matsuda, S. Lee, T. Brylewski, Corrosion behavior of crofer 22APU for metallic interconnects in single and dual atmosphere exposures at 1073 K, Acta Phys. Pol. A 131 (2017) 1394–1398.
[33] P. Gannon, R. Amendola, High-temperature, dual-atmosphere corrosion of solid-oxide fuel cell interconnects, JOM US 64 (2012) 1470–1476.
[34] J.A. Kilner, M. Burriel, Materials for intermediate-temperature solid-oxide fuel cells, Annu. Rev. Mater. Res. 44 (2014) 365–393.
[35] D.J. Young, J. Zurek, L. Singheiser, W.J. Quadakkers, Temperature dependence of oxide scale formation on high-Cr ferritic steels in Ar-H-2-H2O, Corros. Sci. 53 (2011) 2131–2141.
[36] C. Wagner, Oxidation of alloys involving noble metals, J. Electrochem. Soc. 103 (1956) 571–580.
[37] C. Wagner, Reaktionstypen Bei Der Oxydation Von Legierungen, Z. Elektrochem. 63 (1959) 772–790.
[38] R.A. Rapp, The transition from internal to external oxidation and the formation of interruption bands in silver-indium alloys, Acta Metall. Mater. 9 (1961) 730–741.
[39] F. Gesmundo, F. Viani, Transition from internal to external oxidation for binary alloys in the presence of an outer scale, Oxid. Met. 25 (1986) 269–282.
[40] G.H. Meier, K. Jung, N. Mu, N.M. Yanar, F.S. Pettit, J.P. Abellan, T. Olszewski, L. N. Hierro, W.J. Quadakkers, G.R. Holcomb, Effect of alloy composition and exposure conditions on the selective oxidation behavior of ferritic Fe-Cr and Fe-Cr-X alloys, Oxid. Met. 74 (2010) 319–340.
[41] G.R. Holcomb, M. Lukaszewicz, N.J. Simms, B.H. Howard, N.M. Yanar, G.H. Meier, Hydrogen transport during steam oxidation of iron and nickel alloys, Mater. High Temp. (2019) 1–17.
[42] J.H. Swisher, Turkdoga.Et, Solubility permeability and diffusivity of oxygen in solid iron, Trans. Metall. Soc. AIME 239 (1967) 426.
[43] D.P. Whittle, G.C. Wood, D.J. Evans, D.B. Scully, Concentration profiles in underlying alloy during oxidation of iron-chromium alloys, Acta Metall. Mater. 15 (1967) 1747.
[44] J. Takada, S. Yamamoto, S. Kikuchi, M. Adachi, Internal oxidation of Fe-Al alloys in the Alpha-Phase region, Oxid. Met. 25 (1986) 93–105.
[45] J. Takada, M. Adachi, Determination of diffusion-coefficient of oxygen in Alpha-Iron from internal oxidation measurements in Fe-Si alloys, J. Mater. Sci. 21 (1986) 2133–2137.
[46] A.R. Setiawan, M.H. Bin Ani, M. Ueda, K. Kawamura, T. Maruyama, Oxygen permeability through Internal Oxidation Zone in Fe-Cr alloys under dry and humid conditions at 973 and 1 073 K, ISIJ Int. 50 (2010) 259–263.
[47] M.H.B. Ani, T. Kodama, M. Ueda, K. Kawamura, T. Maruyama, The effect of water vapor on high temperature oxidation of Fe-Cr alloys at 1073 K, Mater. Trans. 50 (2009) 2656–2663.
[48] C.G. Lee, Y. Iijima, T. Hiratani, K. Hirano, Diffusion of chromium in Alpha-Iron, Mater. Trans. JIM 31 (1990) 255–261.
[49] R. Braun, M. Fellerkniepmeier, Diffusion of chromium in Alpha-Iron, Physica Status Solidi A Appl. Res. 90 (1985) 553–561.
[50] P.I. Williams, R.G. Faulkner, Chemical volume diffusion coefficients for stainless steel corrosion studies, J. Mater. Sci. 22 (1987) 3537–3542.
[51] A. Inoue, H. Nitta, Y. Iijima, Grain boundary self-diffusion in high purity iron, Acta Mater. 55 (2007) 5910–5916.
[52] H. Falk-Windisch, J.E. Svensson, J. Froitzheim, The effect of temperature on chromium vaporization and oxide scale growth on interconnect steels for Solid Oxide Fuel Cells, J. Power Sources 287 (2015) 25–35.
[53] M.J. Reddy, J.-E. Svensson, J. Froitzheim, Unpublished Work, Chalmers University of Technology, 2020.
[54] P. Huczkowski, N. Christiansen, V. Shemet, J. Piron-Abellan, L. Singheiser, W. J. Quadakkers, Oxidation induced lifetime limits of chromia forming ferritic interconnector steels, J. Fuel Cell Sci. Tech. 1 (2004) 30–34.
[55] P. Huczkowski, V. Shemet, J. Piron-Abellan, L. Singheiser, W.J. Quadakkers, N. Christiansen, Oxidation limited life times of chromia forming ferritic steels, Mater. Corros. 55 (2004) 825–830.
[56] W.J. Quadakkers, J. Piron-Abellan, V. Shemet, L. Singheiser, Metallic interconnectors for solid oxide fuel cells – a review, Mater. High Temp. 20 (2003) 115–127.
[57] D. Caplan, M. Cohen, Scaling of Fe-26Cr alloys at 870°–1200°C, J. Electrochem. Soc. 112 (1965) 471.
[58] D. Caplan, G.I. Sproule, Effect of oxide grain structure on the high-temperature oxidation of Cr, Oxid. Met. 9 (1975) 459–472.
[59] E.A. Gulbransen, K.F. Andrew, Kinetics of the oxidation of chromium, J. Electrochem. Soc. 104 (1957) 334.
[60] P. Kofstad, K.P. Lillerud, Chromium transport through Cr2O3 scales I. On lattice diffusion of chromium, Oxid. Met. 17 (1982) 177–194.
[61] A.C.S. Sabioni, A.M. Huntz, J. Philibert, B. Lesage, C. Monty, Relation between the oxidation growth rate of chromia scales and self-diffusion in Cr2O3, J. Mater. Sci. 27 (1992) 4782–4790.
[62] J. Ehlers, D.J. Young, E.J. Smaardijk, A.K. Tyagi, H.J. Penkalla, L. Singheiser, W. J. Quadakkers, Enhanced oxidation of the 9%Cr steel P91 in water vapour containing environments, Corros. Sci. 48 (2006) 3428–3454.
[63] E. Essuman, G.H. Meier, J. Zurek, M. Hansel, W.J. Quadakkers, The effect of water vapor on selective oxidation of Fe-Cr alloys, Oxid. Met. 69 (2008) 143–162.
[64] A. Chyrkin, P. Huczkowski, V. Shemet, L. Singheiser, W.J. Quadakkers, Sub-scale depletion and enrichment processes during high temperature oxidation of the nickel base alloy 625 in the temperature range 900–1000 °C, Oxid. Met. 75 (2011) 143–166.
[65] J.P. Abelián, Ferritic steel interconnect for reduced temperature SOFC, in: ECS Proceedings Volumes, 2001-16, 2001, pp. 811–819.
[66] E. Essuman, G.H. Meier, J. Zurek, M. Hansel, L. Singheiser, W.J. Quadakkers, Enhanced internal oxidation as trigger for breakaway oxidation of Fe-Cr alloys in gases containing water vapor, Scripta Mater. 57 (2007) 845–848.
[67] H. Kurokawa, Y. Oyama, K. Kawamura, T. Maruyama, Hydrogen permeation through Fe-16Cr alloy interconnect in atmosphere simulating SOFC at 1073 K, J. Electrochem. Soc. 151 (2004) A1264–A1268.
[68] K. Segerdahl, J.E. Svensson, L.G. Johansson, Protective and nonprotective behavior of 11% Cr steel in O-2+H2O environment at 450-700 degrees C, J. Electrochem. Soc. 151 (2004) B394–B398.